Mass fractal dimension from 2D-microscopy images via an aggregation model with variable compactness

Giulia Ferri, Severine Humbert, Jean-Marc Schweitzer, Mathieu Digne, Veronique Lefebvre, Maxime Moreaud

ORIGINAL ARTICLE

Journal Section

Mass fractal dimension from 2D-microscopy images via an aggregation model with variable compactness

Giulia Ferri[1] | **Severine Humbert**[1] | **Jean-Marc Schweitzer**[1] | **Mathieu Digne**[1] | **Veronique Lefebvre**[1] | **Maxime Moreaud**[1,2]

[1]IFP Energies Nouvelles, Solaize, Rhône, 69360, France

[2]CMM MINES ParisTech, PSL-Research University, Fontainebleau, Seine-et-Marne, 77305, France

Correspondence
Giulia Ferri, IFP Energies Nouvelles, Solaize, Rhône, 69360, France
Email: ferrigiulia943gmail.com

Present address
IFP Energies Nouvelles, Solaize, Rhône, 69360, France

Funding information
IFP Energies Nouvelles, Solaize, Rhône, 69360, France

Microscopy-image analysis provides precious information on size and structure of colloidal aggregates and agglomerates. The structure of colloids is often characterized using the three-dimensional mass fractal dimension d_f^{3D}, which is different from the two-dimensional fractal dimension d_f^{2D} that can be computed from microscopy-images. In this work we propose to use a recent morphological aggregation model to find a relationship between 2D image fractal dimension and 3D mass fractal dimension of aggregates and agglomerates. Our case study is represented by scanning transmission electron microscopy-images of boehmite colloidal suspensions. The behaviour of the computed d_f^{3D} at different acid and base concentration shows a fair agreement with the results of Small Angle X-Ray Scattering and with the literature, enabling to use the d_f^{3D} vs d_f^{2D} relationship to study the impact of the composition of the colloidal suspension on the density of colloidal aggregates and agglomerates.

KEYWORDS
fractal dimension, morphological model, image analysis

1 | INTRODUCTION

Image-analysis is frequently used to characterize colloidal particles of silica [1], alumina [2], soot or carbon. These particles can exist as a powder or within liquid suspensions, and they find applications in different domains like electronics, pharmaceutic and

catalysis [3]. Such applications depend on particles size and structure. For this reason the control of aggregation and agglomeration within colloids is of high importance. The mass fractal dimension d_f^{3D} is often used to characterize the structure of aggregates and agglomerates. Assuming that an aggregate/agglomerate consists of N identical spheres of radius a, the fractal dimension enables to link N to the gyration radius R_{gyr} [4;5;6].

$$N = k_f \left(\frac{R_{gyr}}{a} \right)^{d_f^{3D}} \tag{1}$$

where k_f is the fractal pre-factor whose value varies typically between 1 and 1.2, depending on the fractal dimension itself [7]. The mass fractal dimension is close to unity for linear clusters, near to 2 for planar clusters and around 3 for isotropic 3D clusters. d_f^{3D} can be measured by experimental scattering techniques such as Small Angle X-Ray [8] or Neutron [9] Scattering. A change in d_f^{3D} of a colloidal aggregate/agglomerate modifies its density, involving different dispersibility and settling behaviour [10]. This changes the work-ability of a colloidal suspension, as well as the textural properties of the solid obtained after a precipitation or drying process. In the context of γ-alumina catalyst carriers synthesis, the porosity of the final solid depends on the size and shape of the aggregates (meso-porosity $\simeq$ 10 nm) and agglomerates (macro-porosity $\simeq$ 100 nm) resulting from inter-particle interactions during different stages of preparation. By varying the chemical parameters of the colloidal suspension, it is possible to change the aggregation and agglomeration processes [11], leading to different size distribution and fractal dimension. Our interest is to use microscopy-image analysis to study this behaviour, in order to determine the physical-chemical parameters that lead to specific structure change within boehmite suspensions.

A measurement of fractal dimension can be realized from microscopy pictures using the relationship between area and perimeter [12]. This method is widely used in literature [13;14] and enables to obtain directly a two-dimensional fractal dimension d_f^{2D} from the slope of the graph $\log(P^2)$ vs $\log(A)$, where P and A are respectively perimeter and area of the projections. The slope tends to 1 for circular objects and to 2 for linear objects. Since the fractal dimension of the projection d_f^{2D} is different from the mass fractal dimension d_f^{3D}, there is the need of a relationship between these two parameters [15;16;17;18;19].

The aim of our work is to numerically provide such relationship, using a recent morphological aggregation model [20]. The model is used to build clusters with a statistical average fractal dimension, as well as their opaque projections.

2 | DETERMINATION OF 3D-FRACTAL DIMENSION FROM 2D-MISCROPY IMAGES

In this section, we consider an usual standard Scanning transmission electron microscopy (STEM) images of agglomerates of a boemite suspension (on the left in Fig.1) and we explain our step-by-step to extract d_f^{3D} from such images.

2.1 | Image processing and determination of d_f^{2D}

To compute perimeter and area on STEM images, several operations are applied. The image noise is reduced [21;22] by preserving the sharp edges of objects. Morphological TopHat operator [23] on black pixels is applied consisting on morphological opening operator γ and a threshold operator tr_s such that

$$tr_s(I(x)) = \begin{cases} 1 | I(x) > s \\ 0 | I(x) \leq s \end{cases} .$$

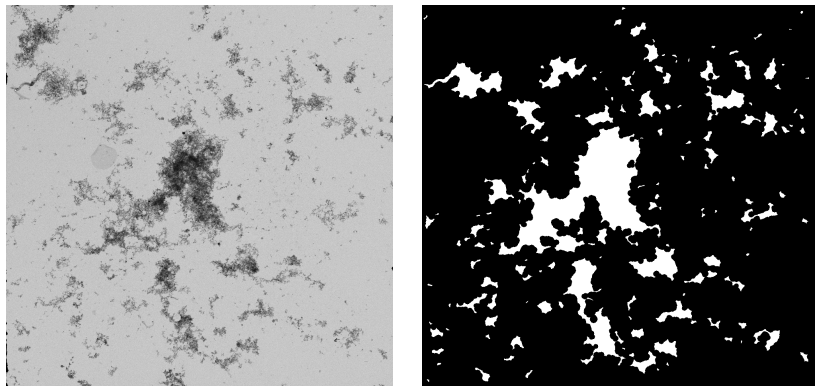

FIGURE 1 Experimental image (on the left) and its binary version (on the right).

Extracted solid suspension can be expressed for an image I as $tr_s(I - \gamma_B(I))$ where s is obtained by inter-class variance maximization on the histogram of I [24], and B is the structuring element which in our case is a disc of radius 30 pixels. Next, two morphological operations of opening γ and closing φ are applied to reduce the remaining noise, defined for the image I and the structuring element C as $\gamma_C(I) = \delta_C(\varepsilon_C(I))$ and as $\varphi_C(I) = \varepsilon_C(\delta_C(I))$ where δ and ε are respectively morphological dilation and erosion [23], C is a disc of diameter 6 pixels. A final step of image cleaning consists in a hole filling and in the removal of the objects touching the edges of the image [23]. The holes are not always related to the existence of a real hole but rather to variations in thickness. While objects touching the borders would provide a misleading perimeter and area. Fig.1 reports an example of an experimental image and of the final binary image. On the binary images it is possible to calculate the perimeter P and area A of each object. The d_f^{2D} is estimated from the angular coefficient of the line interpolating the experimental points on the plot $\log(P^2)$ vs $\log(A)$ [12]. To estimate the d_f^{3D} corresponding to a given d_f^{2D} it is necessary to pass through a morphological model.

2.2 | Morphological aggregation model

The morphological aggregation model [20] builds clusters consisting of a N number of non-overlapping elementary objects arranged according to a given statistical average fractal dimension d_f^{3D}. Clusters are built by sequential addition, assigning a different sticking probability to the points on the cluster. In particular, "concave points", leading to compact clusters, are distinguished from "non-concave" points, leading to loose structures. In addition the concave points closest to the centre of mass of the cluster are distinguished as well, in these points the maximum compactness is reached. The model enables to obtain clusters with a fractal dimension d_f^{3D} between 1.3 and 3. A fast scheme is available in case of spheres [20] and is used in this present work. A new object P is stuck to the already present cluster A either in a point on the cluster dilation

$$X_P = F(\delta_P(A)), \tag{2}$$

either on a concave point of the dilation

$$X_P^{CV} = F\left(\delta_P(A)\right) \cap F\left(\frac{\varphi_r(\delta_P(A))}{\delta_P(A)}\right) \tag{3}$$

or in the concave point closest to the center of mass of A

$$X_P^M = x \in X_P^{CV} | \inf d(x, M). \tag{4}$$

$F(X)$ is the set of points at the border of X, $F(X) = \{z : B_z \cap \check{X} \neq \emptyset\}$, with B unit ball, M is the center of mass of the cluster A and $d(x, M)$ is the euclidean distance between the position x of the concave point and M.

2.3 | Construction of d_f^{3D} vs d_f^{2D} chart

In order to compute d_f^{2D} of a cluster generated by the model, it is necessary to generate the projections of numerous clusters for a given d_f^{3D} in the largest range for N (the number of elementary spheres). The mass fractal dimension d_f^{3D} of each cluster is determined with Eq.(1). In the present study a fractal pre-factor k_f of 1.2 is used, in order to establish reference values for d_f^{3D} of the clusters generated [20]. The model inlet parameters where chosen in order to obtain a target statistical average $\overline{d_f^{3D}}$. Only the clusters with $\left|d_f^{3D} - \overline{d_f^{3D}}\right| \leq 0.01$ were used to compute the projection. For each cluster, one orthogonal projection is computed, since a large number of simulations is performed it is possible to assume that area and perimeter computed on the projection are anisotropic. Fig.2 represents three-dimensional clusters with their projection for different number of elementary spheres N. A hole filling operation is performed to obtain projection comparable to experimental images [23]. The computation of area and perimeter enables the construction of the $\log(P^2)$ vs $\log(A)$ plot, whose slope is d_f^{2D} [12].

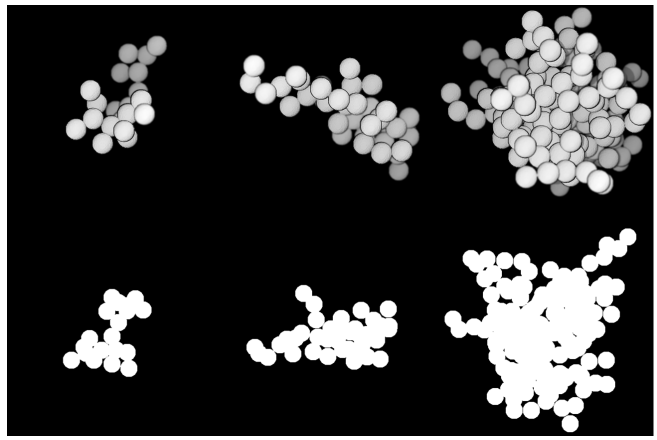

FIGURE 2 Illustration of three-dimensional clusters and their projections for $\alpha = \beta = 0.1$ and $N = 20, 40, 160$. α and β are the compactness parameters of the morphological aggregation model, more details are in Ferri et al. [20].

2.4 | Relationship between d_f^{3D} and and d_f^{3D}

In Fig.3(a) tha aggregation morphological model is used to compute the d_f^{3D} vs d_f^{2D} chart. The higher is d_f^{3D}, the lower is the d_f^{2D} of its projection, similar results were obtained by Ehrl et al. [19], with a linear relationship between the two parameters. In our

case a polynomial of third degree represents more accurately the results

$$d_f^{3D} = 6.03 \cdot (d_f^{2D})^3 - 25.63 \cdot (d_f^{2D})^2 + 34.13 \cdot d_f^{2D} - 11.55. \tag{5}$$

The coefficients of the polynomial minimize least-squares fit.

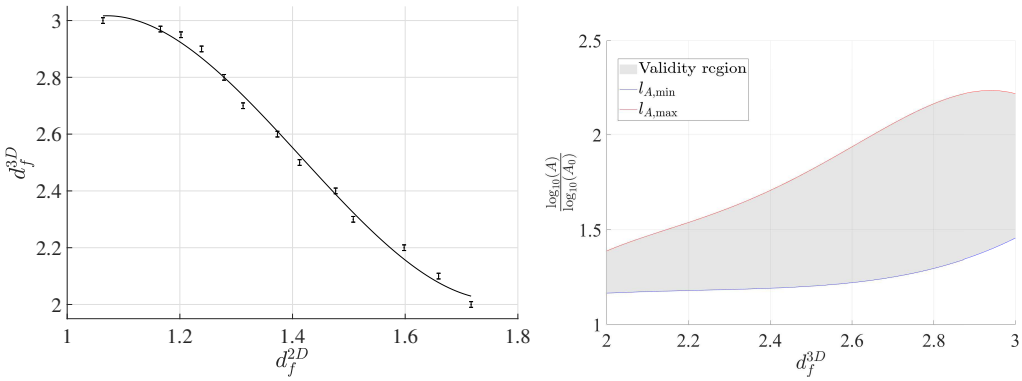

(a) d_f^{3D} vs d_f^{2D} chart

(b) chart limits

FIGURE 3 d_f^{3D} vs d_f^{2D} relationship described in Eq.(5) in (a) and its validity in terms of surface area A in (b).

2.5 | Validity region

To compare experimental and model projections, the perimeter-area plots are represented as $\log(P^2)$ vs. $\log(A)/\log(A_0)$, where A_0 is the projection of the elementary object forming the cluster. Aggregation simulations were performed with a sphere of radius 10 pixels, corresponding to an opaque projection of area A_0 of 380 pixels. This is important so that the relationship shown in Fig.3(a) does not depend on the size scale and unit of measurement. The Eq.(5) is valid within limits, in terms of projected $\log(A)/\log(A_0)$, for a given d_f^{3D}. The lower and the upper limit (respectively $l_{A,\min}$ and $l_{A,\max}$) are reported as reachable limit ranges by the aggregation model. The upper limit is also due to the maximum simulation volume, which in our case is of 10^9 voxels for time computing constraints.

The lower and the upper limits can be described as a function of d_f^{3D} fitting respectively the lowest and the highest $\log(A)/\log(A_0)$ of the opaque projections of the simulated clusters.

$$\begin{aligned} l_{A,\min} &= 0.26 \cdot (d_f^{3D})^4 - 1.99 \cdot (d_f^{3D})^3 + 5.57 \cdot (d_f^{3D})^2 - 6.64 \cdot d_f^{3D} + 3.90 \\ l_{A,\max} &= -2.78 \cdot (d_f^{3D})^4 + 26.43 \cdot (d_f^{3D})^3 - 93.46 \cdot (d_f^{3D})^2 + 146.41 \cdot d_f^{3D} - 84.63. \end{aligned} \tag{6}$$

The validity region and its limits are represented in Fig.3(b). A_0 does not influence the results for d_f^{2D}, but only the validity interval of the relationship in Eq.(5) on the $\log(P^2)$ vs. $\log(A)/\log(A_0)$ plot.

3 | EXPERIMENTAL APPLICATION TO BOEHMITE SUSPENSIONS

In this section, we use the relationship between d_f^{3D} and d_f^{2D} to compute the mass fractal dimension from STEM images of different boehmite suspensions. Results are compared to Small Angle X-Ray Scattering and literature.

3.1 | Boehmite suspensions preparation

Boehmite suspension are prepared with a highly dispersible powder from Sasol GmbH whose crystallites have the geometry of a rectangular beam with dimensions 5.2, 8.1 and 2.4 nm. These values are obtained from the X-Ray diffractogram using generalized Debye equation [2]. The colloidal suspensions are prepared with different concentration of 1M Fisher Scientific nitric acid (J/5550/PB15) and 1M Chem-Lab ammonia (CL05.0101.1000). The powder concentration is kept at 0.02 g/L in order to minimize overlapping in STEM images. The composition of the samples is shown in Tab.1. The table also reports the measured pH (Mettler-Toledo Seven2Go pH meter). A2 and B0 are the same suspension, which represents the initial conditions before ammonia addition (samples B1-3).

3.2 | STEM Images Acquisition

A droplet of 10 µL of the suspension is deposited on copper grids with carbon membranes without holes and dried under IR lamp. After 2 min, the excess water is drawn off with a tissue paper.

The samples are characterized with Scanning Transmission Electron Microscope (STEM), using a FEI Nova NanoSEM microscope operating at 15keV.

The different chemical parameters of the suspensions (acid and base concentration) of the samples causes the formation of structures ranging within a wide size range (10 nm - 10 µm). For this reason, the magnification level for a given sample is chosen in order to visualize the largest objects in their entirety. In particular we use a magnification of X 50000 for the samples A0, A1, A2 and A3, and a magnification of X 1500 is used for B1, B2 and B3.

3.3 | Small Angle X-Ray Scattering

The analyses were performed at the SWING beamline at synchrotron SOLEIL in Saint Aubin, France. The boehmite suspensions are placed in a stirred reactor, from which the sample is pumped continuously through a quartz capillary of 1.5 mm, crossed by the X-ray beam, whose incident energy is 10 keV. The experiments are realized on an initial boehmite suspension analogous to the A2-B0 at 1g/L. The SAXS curves measured 30 min after the base injection are fit with Beaucage model [26] in order to compute the mass fractal dimension.

3.4 | Monitoring of boehmite dispersion upon acid addition

The aggregates (observed in the samples A0, A1, A2 and A3) have an average diameter D between 20 and 40 nm (Tab.1). For these objects A_0 is the one of an elementary crystallite. The average surface of the opaque projection of the crystallite is 38.25 nm^2, obtained by averaging on 1000 projections considering random 3D orientations [27] with a precision of 0.1 nm/voxels.
We report the STEM images of the aggregates at different acid concentrations and their corresponding $\log(P^2)$ vs $\log(A)/\log(A_0)$ plots in Fig.4.

The grey regions in these graphs refer to the validity limits of the d_f^{3D} - d_f^{2D} relashionship (Fig.3).
The results of d_f^{2D} and d_f^{3D} (computed with Eq.(5)) are reported in Tab.1. The dispersion in acid leads to an increase in d_f^{2D},

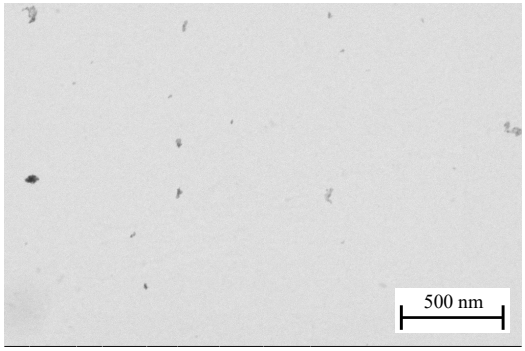

(a) STEM image of A0

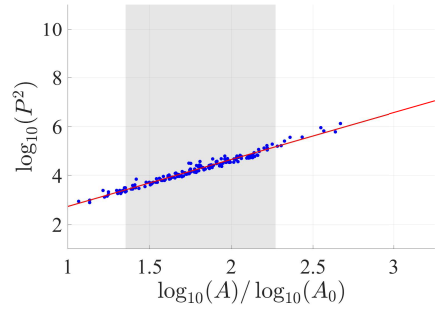

(b) log(P) vs log(A) plot of A0

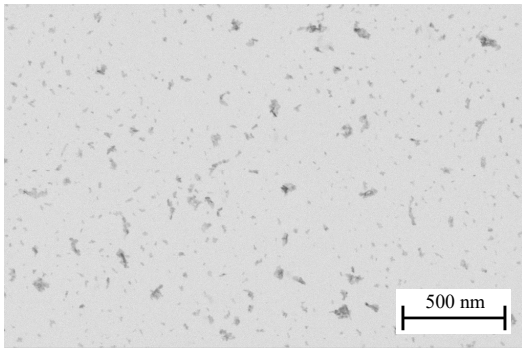

(c) STEM image of A1

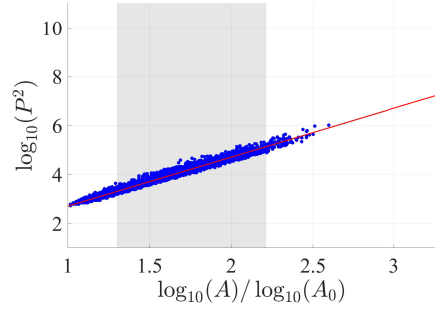

(d) log(P) vs log(A) plot of A1

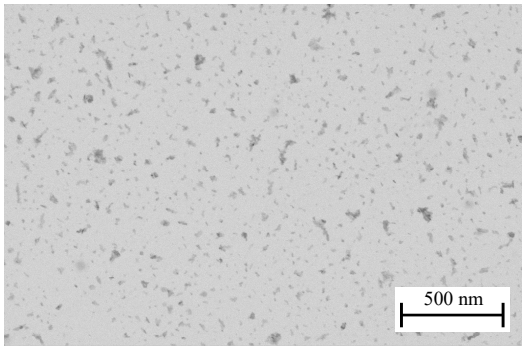

(e) STEM image of A2-B0

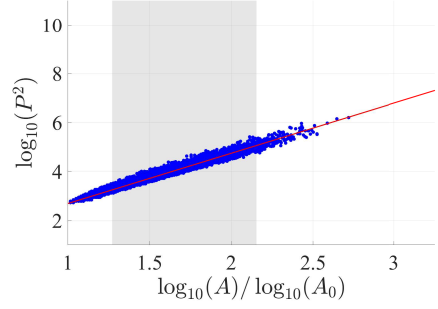

(f) log(P) vs log(A) plot of A2-B0

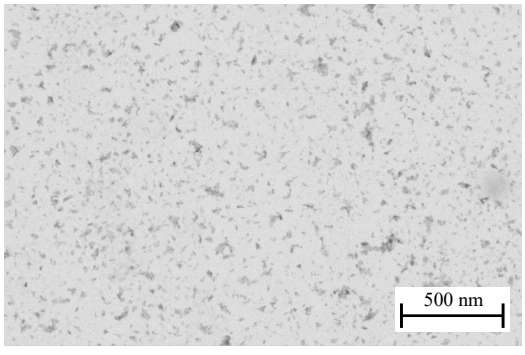

(g) STEM image of A3

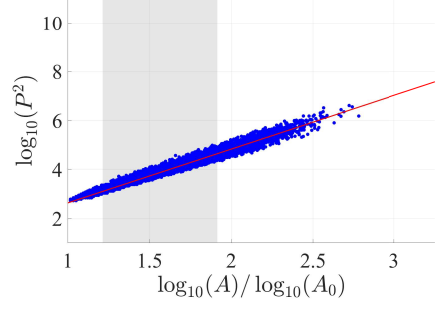

(h) log(P) vs log(A) plot of A3

FIGURE 4 STEM images and $\log(P^2)$ vs $\log(A)$ plots of boehmite suspensions for varying acid content

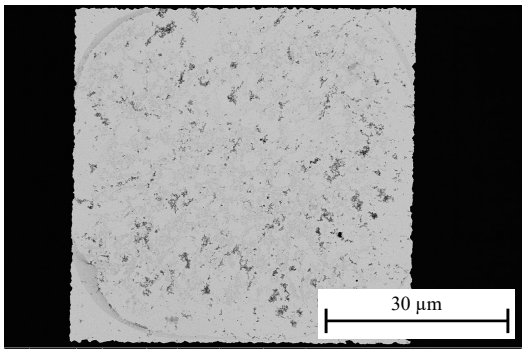

(a) STEM image of B1

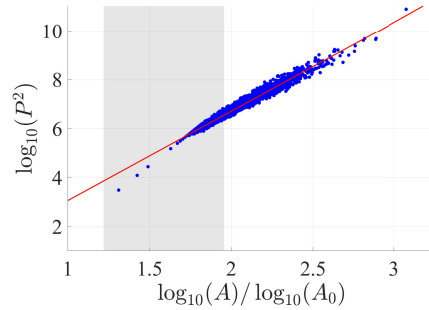

(b) log(P) vs log(A) plot of B1

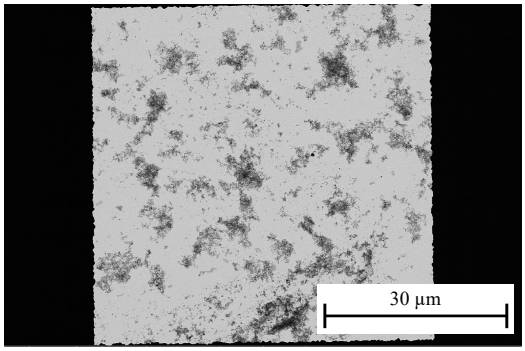

(c) STEM image of B2

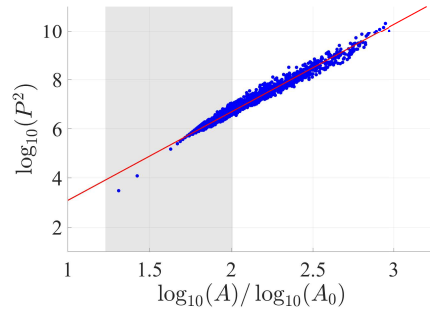

(d) log(P) vs log(A) plot of B2

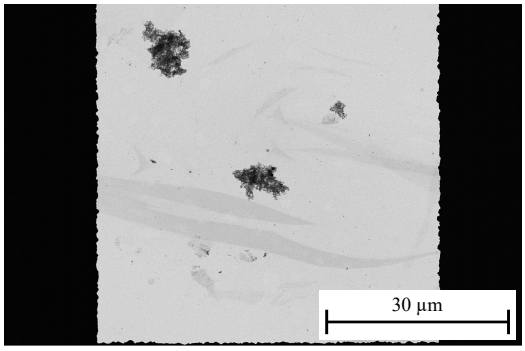

(e) STEM image of B3

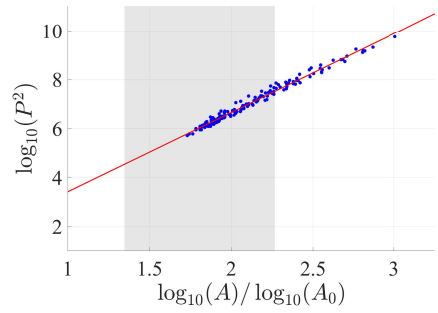

(f) log(P) vs log(A) plot of B3

FIGURE 5 STEM images and $\log(P^2)$ vs $\log(A)$ plots of boehmite suspensions for varying base content

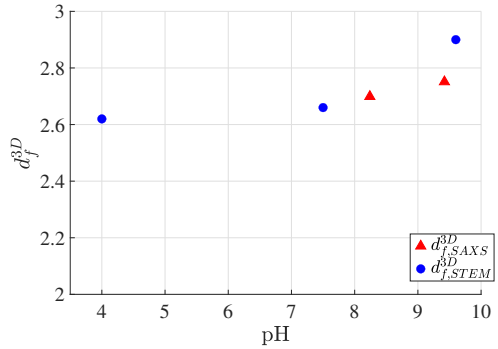

FIGURE 6 d_f^{3D} computed via image analysis and Eq.(5), and measured with Small Angle X-Ray Scattering at different pH.

indicating the formation of loose structures. This is in agreement with d_f^{3D}, and quite visible from the STEM images. The objects present in A3 are more elongated than the ones in A0-1. We observe a change of around 0.3 units of d_f^{3D}. The difference between A3 and A2 is less noticeable, but the image processing enables to identify it. In conclusion, the acid content decreases fractal dimension of the boehmite suspension as it has been observed in other research works [28].

3.5 | Monitoring of boehmite agglomeration upon basic addition

In a similar way, the relationship between d_f^{3D} and d_f^{2D} is used to characterize objects of a bigger scale, the agglomerates (in samples B1-3), obtained by ammonia addition to the suspension A2-B0. The average diameter D is of several hundreds of nanometers (Tab.1). In this case, the elementary particle is the aggregate, and A_0 was taken as the average area of the dispersed sample A2-B0, which is 453 nm^2. We now focus on the STEM images in Fig.5. The effect of the base content seems to favour the formation of more compact structures with a decrease in d_f^{2D}. Between samples B1-2 and B3, we notice an evident change in the structure. Sample B3 presents highly compact objects Fig.5(e), for which the mass fractal dimension is 2.9. For B3 the pH is close to the Point of Zero Charge (PZC) of the suspension [29]. In these conditions the agglomeration is typically favoured [30]. We were able to observe an increase in the mass fractal dimension towards the PZC also with *in-situ* Small Angle X-Ray Scattering (Fig.6).

TABLE 1 Composition, fractal dimension and average diameter of the boehmite suspension samples

Sample Name	HNO_3 [mM]	NH_3 [mM]	pH	d_f^{2D}	d_f^{3D}	D [nm]
A0	0	0	5.6	1.21	2.91	37
A1	0.75	0	3.4	1.26	2.83	22
A2-B0	1.5	0	2.9	1.3	2.76	21
A3	37.5	0	2.6	1.39	2.57	25
B1	1.5	1.9	4	1.37	2.62	682
B2	1.5	2.2	7.5	1.35	2.66	915
B3	1.5	3.2	9.6	1.22	2.90	1122

4 | CONCLUSION

The presented work provides a strategy to compute mass fractal dimension from two-dimensional microscopy images. A relationship between d_f^{2D} and d_f^{3D} is numerically found using a recent morphological aggregation model. The mass fractal dimensions we obtained are in fair agreement with a visual estimate, enabling to use STEM images to determine the impact of different operating conditions on the structure of aggregates and agglomerated formed within a colloidal suspension. This allows a better insight of the physical-chemical aspects that produce such structures In particular, we observed that an increase in acid concentration, causes the formation of more loose structures, with a decrease in d_f^{3D}. While the increase of base content leads to more compact structures, leading to higher d_f^{3D}. A complete validation of our approach is achieved by comparison of our results for boehmite suspension at different acid and base contents, with the literature and Small Angle X-Ray Scattering experiments.

REFERENCES

[1] Nelson Ibaseta and Béatrice Biscans. Fractal dimension of fumed silica: Comparison of light scattering and electron microscope methods. *Powder Technology*, 203(2):206–210, 2010. ISSN 00325910. doi: 10.1016/j.powtec.2010.05.010.

[2] David Chiche, Mathieu Digne, Renaud Revel, Corinne Chanéac, and Jean-Pierre Jolivet. Accurate determination of oxide nanoparticle size and shape based on X-ray powder pattern simulation: Application to boehmite AlOOH. *The Journal of Physical Chemistry C*, 112(23):8524–8533, 2008. ISSN 1932-7447. doi: 10.1021/jp710664h.

[3] Harald Brune, Holger Ernst, Armin Grunwald, Werner Grünwald, Heiri Hofmann, Harald Krug, Peter Janich, Marcel Mayor, Wolfgang Rathgeber, Günter Schmid, Ulrich Simon, Viola Vogel, and Daniel Wyrwa. *Nanotechnology: Assessment and Perspectives*. Springer-Verlag Berlin Heidelberg, 2006. ISBN 978-3-540-32819-3. doi: 10.1007/3-540-32820-3.

[4] Pramod Kulkarni, Paul A. Baron, Christopher M. Sorensen, and Martin Harper. *Nonspherical Particle Measurement: Shape Factor, Fractals, and Fibers*, chapter 23: 507–547. John Wiley & Sons, Ltd, 2011. ISBN 9781118001684. doi: https://doi.org/10.1002/9781118001684.ch23. URL `https://onlinelibrary.wiley.com/doi/abs/10.1002/9781118001684.ch23`.

[5] Stephen R Forrest and Thomas A Witten Jr. Long-range correlations in smoke-particle aggregates. *Journal of Physics A: Mathematical and General*, 12(5):L109–L117, 1979.

[6] A V Filippov, Mauricio Zurita, and Daniel E Rosner. Fractal-like aggregates: Relation between morphology and physical properties. *Journal of Colloid and Interface Science*, 229(1):261–273, 2000. ISSN 0021-9797. doi: 10.1006/jcis.2000.7027.

[7] Christopher M Sorensen and Gregory C Roberts. The prefactor of fractal aggregates. *Journal of Colloid and Interface Science*, 186:447–452, 1997.

[8] Eugen Mircea Anitas. Small-angle scattering from fractals: Differentiating between various types of structures. *Symmetry*, 12(1): 65, 2020. doi: 10.3390/sym12010065.

[9] Jose Teixeira. Small-angle scattering by fractal systems. *Journal of Applied Crystallography*, 21(6):781–785, 1988. ISSN 0021-8898. doi: 10.1107/S0021889888000263.

[10] Nelson Ibaseta and Beatrice Biscans. Ultrafine aerosol emission from the free fall of TiO_2 and SiO_2 nanopowders. *Powder and Particle*, 25(0):190–204, 2007.

[11] Lawrence M Anovitz, Xin Zhang, Jennifer Soltis, Elias Nakouzi, Anthony J Krzysko, Jaehun Chun, Gregory K Schenter, T R Graham, Kevin M Rosso, James J De Yoreo, Andrew G Stack, Markus Bleuel, Cedric Gagnon, David F R Mildner, Jan Ilavsky, and Ivan Kuzmenko. Effects of ionic strength, salt, and pH on aggregation of boehmite nanocrystals: Tumbler small-angle neutron and x-ray scattering and imaging analysis. *Langmuir*, 34:15839–15853, 2018. doi: 10.1021/acs.langmuir.8b00865.

[12] Benoit B Mandelbrot, Dann E Passoja, and Alvin J Paullay. Fractal character of fracture surfaces of metals. *Nature*, 308:721–722, 1984.

[13] Bingqiao Yang, Pengliang Huang, Shaoxian Song, Huihua Luo, and Yi Zhang. Hydrophobic agglomeration of apatite fines induced by sodium oleate in aqueous solutions. *Results in Physics*, 9:970–977, 2018. ISSN 22113797. doi: 10.1016/j.rinp.2018.03.049.

[14] Huijuan Xiu, Feiyan Ma, Jinbao Li, Xin Zhao, Lihua Liu, Pan Feng, Xue Yang, Xuefei Zhang, Evguenii Kozliak, and Yun Ji. Using fractal dimension and shape factors to characterize the microcrystalline cellulose (mcc) particle morphology and powder flowability. *Powder Technology*, 364:241–250, 2020. ISSN 00325910. doi: 10.1016/j.powtec.2020.01.045.

[15] Jenny A Nelson, Roy J Crookes, and S Simons. On obtaining the fractal dimension of a 3D cluster from its projection on a plane-application to smoke agglomerates. *Journal of Physics D: Applied physics*, 23(4):465–468, 1990.

[16] Ümit Ö Köylü, Gerard M Faeth, Tiago L Farias, and M Graça Carvalho. Fractal and projected structure properties of soot aggregates. *Combustion and Flame*, 100, 1995.

[17] C Oh and Christopher M. Sorensen. The effect of overlap between monomers on the determination of fractal cluster morphology. *Journal of Colloid and Interface Science*, 193(1997):17–25. ISSN 0021-9797.

[18] Augusto M Brasil, Tiago L Farias, and M Graça Carvalho. A recipe for image characterization of fractal-like aggregates. *Journal of Aerosol Science*, 30:1379–1389, 1999.

[19] Lyonel Ehrl, Miroslav Soos, and Marco Lattuada. Generation and geometrical analysis of dense clusters with variable fractal dimension. *The Journal of Physical Chemistry B*, 113(31):10587–10599, 2009. ISSN 1520-6106. doi: 10.1021/jp903557m.

[20] Giulia Ferri, Severine Humbert, Mathieu Digne, and Jean-Marc Schweitzer. Aggregation morphological model with variable compactness: application to colloidal system. Submitted to Image Analysis and Stereology, online on hal: https://hal.archives-ouvertes.fr/hal-03033506v1.

[21] Michiyoshi Kuwahara, Kozaburo Hachimura, Eiho S, and Masato Kinoshita. *Processing of RI-Angiocardiographic Images*, pages 187–202. Springer US, Boston, MA, 1976. ISBN 978-1-4684-0769-3. doi: 10.1007/978-1-4684-0769-3_13. URL `https://doi.org/10.1007/978-1-4684-0769-3_13`.

[22] Mark A Schulze and John A Pearce. A morphology-based filter structure for edge-enhancing smoothing. In *Proceedings of 1st International Conference on Image Processing*, pages 530–534, 1994.

[23] Serra Jean. Introduction to morphological filters. *Image analysis and mathematical morphology*, 2:101–114, 1988.

[24] Nobuyuki Otsu. A threshold selection method from gray-level histograms. *IEEE Transactions on systems, man and cybernetics*, 9:62–66, 1979.

[25] Dale W Schaefer and Alan J Hurd. Growth and structure of combustion aerosols: Fumed silica: Fumed silica. *Aerosol Science and Technology*, 12(4):876–890, 1990. ISSN 0278-6826.

[26] Gregory Beaucage and Dale W Schaefer. Structural studies of complex systems using small-angle scattering: a unified guinier/power-law approach. *Journal of Non-Crystalline Solids*, 172 –174:797–805, 1994. ISSN 00223093.

[27] Maxime Moreaud, Dominique Jeulin, Vincent Morard, and Renaud Revel. TEM image analysis and modelling: application to boehmite nanoparticles. *Journal of Microscopy*, 245(2):186–99, 2012.

[28] Lucie Speyer, Séverine Humbert, Thomas Bizien, Vincent Lecocq, and Antoine Hugon. Peptization of boehmites with different peptization index: An electron microscopy and synchrotron small-angle x-ray scattering study. *Colloids and Surfaces A: Physicochemical and Engineering Aspects*, 603:125175, 2020. ISSN 09277757. doi: 10.1016/j.colsurfa.2020.125175.

[29] Marek Kosmulski. pH-dependent surface charging and points of zero charge. IV. Update and new approach. *Journal of Colloid and Interface Science*, 337(2):439–448, 2009. ISSN 0021-9797. doi: 10.1016/j.jcis.2009.04.072.

[30] Evert Johannes Willelm Verwey and Jan Theodoor Gerard Overbeek. *Theory of the stability of lyophobic colloids: the interaction of sol particles having an electric double layer*. Elsevier publishing company Inc., 1948.